Surface-enhanced Raman spectroscopy for tellurium detection by AgNPs-loaded 3D porous graphene hydrogel

Xiaojiao Zhou[1,2], *Jianwei Gao*[1], *Hua Huang*[1], *Qingsheng Wu*[1], *Xiang Ji*[1] ✉

[1]*Key Laboratory of Neutronics and Radiation Safety, Institute of Nuclear Energy Safety Technology, Chinese Academy of Science, Hefei, People's Republic of China*
[2]*University of Science and Technology of China, Hefei, People's Republic of China*
✉ *E-mail: xiang.ji@fds.org.cn*

Published in Micro & Nano Letters; Received on 2nd May 2017; Revised on 16th June 2017; Accepted on 4th July 2017

A three-dimensional (3D) graphene hydrogel covered by uniform silver nanoparticles as an effective substrate for surface-enhanced Raman scattering application was fabricated by facile ethylenediamine-induced self-assembly method. The anchor of silver nanoparticles endows the enhanced Raman spectroscopy with the sensitivity and multiplex requirements for the tellurium quick detection using the robust graphene-based monoliths. The porous structure offers essential channels and space for Te(IV) access. After exposure to Te(IV), the distinguished peak of Te-O at 584.9 cm^{-1}, which was enhanced significantly and kept constant over a wide range of pH, was selected as the indicative of Te(IV) level. At the optimal pH, the concentration dependent surface-enhanced Raman spectroscopy shows that the detection limit was as low as 100 nM.

1. Introduction: ^{210}Po, the most hazardous pollutants in terms of its severe toxic and radioactive effects on both ecological environment and human health [1], is an important radionuclide produced by neutron capture on ^{209}Bi in lead-bismuth cooled reactors. It can enter into the water circulation system and threat the ecological environment security seriously under nuclear accident conditions. Therefore, it is highly valuable to develop a quick and sensitively analytical method for the radioactive ^{210}Po. Recently, due to the advantages of the ultra-high sensitivity, high resolution, fluorescence-quenching characteristic, non-destructive detection [2], and fingerprint information of the chemical structure, the surface-enhanced Raman scattering (SERS) has been widely used in detection of low-level harmful and toxic substance, such as melamine [3], pesticides [4], trinitrotoluene [5] and so on. AgNPs possess the Raman enhancing properties because of its unique surface plasmons resonance [6]. The combination of graphene and silver nanoparticles (AgNPs) has aroused research in the field of SERS detection for their common qualities in enhancing Raman spectroscopy [7, 8]. Based on the formation of charge transfer states of the AgNPs-adsorbed uranyl ions complex and the excitation of transverse collective electron resonances on the surface of AgNPs, it has also been used in detection of trace uranium [9, 10]. In addition, the specific ability of metallic Ag to selective accumulate Po has also been documented [11]. At this point, the AgNPs/graphene is also the best choice of SERS substrate for ^{210}Po detection. In contrast to the conventional two-dimensional AgNPs/graphene composites, the three-dimensional (3D) frameworks provides convenience for the separation and replacement. Moreover, the porous structure also offers the access for the diffusion of ions and molecules. These characteristics render it unique superiority in promoting detection of radionuclides for nuclear accident emergency. However, to our best knowledge, there are very few works about SERS detection of radionuclide using the porous AgNPs/graphene monolith [12], much less in detection of radioactive ^{210}Po.

Te, a lighter homologue of Po, has non-radioactive isotope and can be handled easily. It is always used as a surrogate of Po for their similar chemical properties [13, 14]. Po in water solution mainly exists in the form of quadrivalent state (Po(IV)) [15], which is similar to Te(IV) in the chemical behaviour as demonstrated in previous study [16]. In this work, employing the robust AgNPs/graphene hydrogel (rGO-Ag_H) and homologue Te(IV), the enhanced sensitivity for quick SERS detection is discussed in terms of the effective decoration of AgNPs and the interactions between the AgNPs and Te(IV) species.

2. Materials and methods: The previously reported Te(IV) stock solution was used in the experiments [11]. The AgNPs/graphene hydrogel was fabricated by ethylenediamine (EDA)-reduction induced self-assembly method. In a typical process, 0.505 g of graphene oxide (GO) and 0.25 g of $AgNO_3$ were mixed in deionised (DI) water under the ultrasonic condition, and then 40 µl of EDA was added to 5 ml of the mixture in a 50 ml vial and reacted at 90 °C for 20 h. The rGO-Ag_H was obtained after soaking the resulting hydrogel in DI water for 48 h. The water was replaced every 6 h to remove the residual silver ions in the rGO-Ag_H. To measure the mechanical strength, the cylindrical rGO-Ag_H was prepared by 30 ml of the mixture and 240 µl of EDA. The cylinder was freeze-dried and the two cross sections were cut into paralleled.

In Te(IV) detection experiments, the hydrogel was put into a polyethylene tube filled with Te(IV) solution. The pH of the system was adjusted with negligible volumes of 5 or 0.5 mol/l NaOH, and the mixture suspension was reacted by shaking for several hours at 30°C (160 rpm). After that, the hydrogel was separated and the supernatant was assayed for residual Te(IV). All experiments were conducted for three times to ensure the reproducibility.

The compressive strength was measured using an Instron E3000 universal testing machine. Microstructure was observed by scanning electron microscopy (SEM) on a Carl Zeiss ΣIGMA. The morphology of AgNPs was explored by a Tecnai G2 F20 S-TWIN transmission electron microscope (TEM) coupled with an energy dispersive spectrometer (EDS). The UV-vis absorption spectra of samples that were dispersed in deionised water were obtained using a Shimadzu UV 2600 spectrophotometer. The alternation of functional groups was characterised by a Nicolet 8700 Fourier transform infrared spectrometer in the range of 4000–500 cm^{-1} with a resolution of 1 cm^{-1} for three times, using KBr pellet technique. The chemical states of elements were investigated by an ESCALAB 250 X-ray photoelectron spectroscopy (XPS). SERS measurements were carried out on a Horiba Jobin

Yvon LabRAM Raman microprobe using a 633.0 nm excitation wavelength.

3. Results and discussion: A digital photograph of the as synthesised freeze-dried rGO-Ag_H with cake shape shows an intact structure in the macroscopic appearance (Fig. 1*a*). When supporting a glass dish with the weight of 16 g, which is more than 800 times over the sample's weight, it is compressed thoroughly (Fig. 1*b*). However, after the compression is released, the sample remains intact and is basically recovered to its original shape (Fig. 1*c*), indicating the exceptional resilience of the freeze-dried rGO-Ag_H even if losing of the hydrogen-bond interactions [17]. Van der Waals' forces and π–π attraction, which facilitates the stacking and agglomeration of graphene sheets, have been confirmed to be the main force of forming a 3D structure through chemical reduction-induced self-assembly method. Both of these two forces can be can be further enhanced as a result of reduction [18].

The mechanical strength of the freeze-dried rGO-Ag_H is also high. Fig. 1*d* displays the uniaxial compression test of the cylindrical aerogel at different set strains. The compressive strain–stress curve shows a horizontal linear region at stain below 45%, and a plateau with gradually increasing slope until very large compressive strain up to 91%. According to the calculation from the curve, the maximum compressive strength of freeze-dried rGO-Ag_H measured at 96% of the maximum compressive strain is ~12 kPa. It is comparable with the published result of Ling Qiu *et al.*, in which the compressive stress at 80% strain of assembled aerogel by freeze casting method was 18 kPa [18]. Li *et al.* [19] also reported that the compressive strength of graphene aerogel prepared by the same method ranged from 4.0 to 5.9 kPa, prompting the speculation that the enormous difference may be resulted from the attachment of AgNPs. The excellent mechanical property, which can ensure the integrity of rGO-Ag_H in the adsorption process, is favourable for simplifying the procedure of sample separation in tellurium detection process.

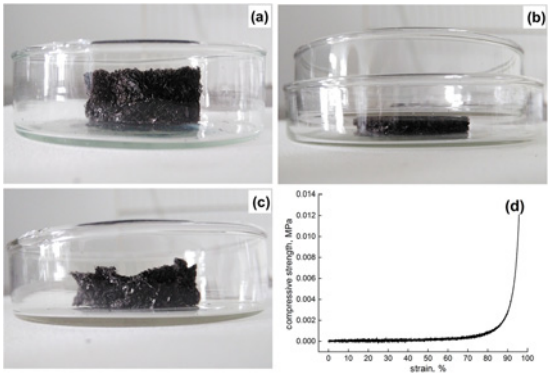

Fig. 1 *Images of freeze-dried rGO-Ag_H (prepared by 5 ml mixture)*
a Before compression
b In compression
c After compression and
d Compressive strain-stress curve of cylindrical sample prepared by 25 ml mixture at the first cycle

The SEM image of the freeze-dried rGO-Ag_H displays continuous porous structure with the average pore size of 40 µm (Fig. 2*a*), which plays the dual role in providing channels for the access of heavy metal ions and increasing the contact area. The TEM analysis of the graphene sheets reveals the compact distribution of AgNPs (Fig. 2*b*). It has been reported that the SERS effectiveness of silver can be explained by two distinct enhancement mechanisms: short-range chemical enhancement and long-range electromagnetic enhancement (EM) [20]. The long-range EM enhancement of magnitude required to explain single-molecule SERS cannot be induced by spherical or nanocrystal-shaped single particles [21]. Hence it can be speculated that the AgNPs distributed closely can act as the 'hot spots', which is the most desirable sites for SERS enhancement. The close stacked distribution of the AgNPs (indicate by white arrows), caused by the overlapping of reduced GO (rGO) sheets, is also observed in the TEM image. The EDS characterisation of the small white square confirmed the successful attachment of AgNPs on the rGO sheets (inset in Fig. 2*c*). The statistical analysis of AgNPs in the big white square under high magnification (Fig. 2*c*) shows that the diameters of AgNPs on the surface of rGO are in the range of 9.0–60.0 nm (Fig. 2*d*). The mean diameter is calculated to be 25.7 ± 2.0 nm in size. The XRD pattern of the rGO-Ag_H in Fig. 2*e* illustrates the face-centred cubic crystal structure of AgNPs [22, 23]. The diffraction peak for Ag(220) is used to estimate the size of AgNPs by the Scherrer's equation [24]:

$$n = 0.89\lambda/(\beta \cos\theta) \quad (1)$$

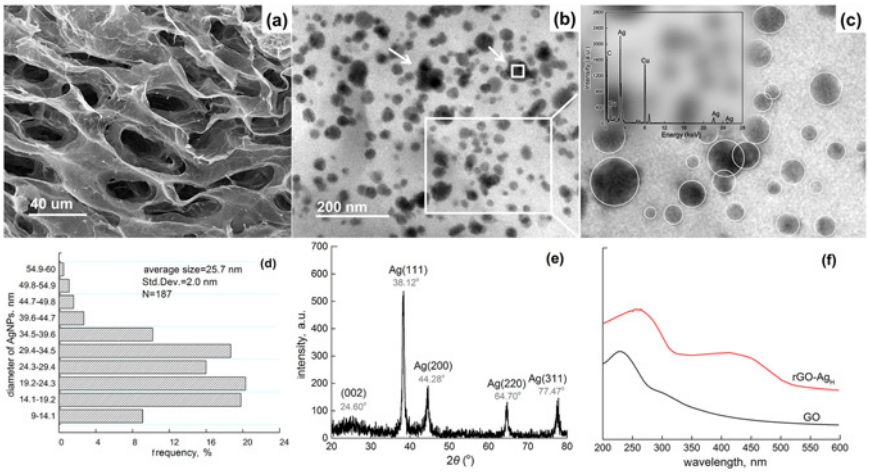

Fig. 2 *SEM image of the freeze-dried rGO-Ag_H displays continuous porous structure with the average pore size of 40 µm of rGO-Ag_H*
a SEM images (a),
b and c TEM-EDS characterisation,
d Size distribution of AgNPs,
e XRD (e) and
f UV-vis spectra

doi: 10.1049/mnl.2017.0297

where λ is the X-ray wavelength used in XRD characterisation and is equal to 0.154 nm here, β is the full width at half-maximum of the XRD profile and θ is the Bragg angle. The average size of Ag on rGO sheets is calculated to be ~28 nm, which is consistent with the TEM results above. In addition, a broad peak appears at 2θ of 24.60°, corresponding to the graphitic planes of (002). The d_{002} spacing, which results from the turbostratic stacking of reduced GO sheets, is calculated to be ~0.36 nm. It is close to the value of pristine graphite (0.34 nm) [25], suggesting the reduction of GO and the re-establishment of conjugated graphene network (sp^2carbon) [26]. Fig. 2*f* shows the UV-vis spectra of GO and rGO-Ag_H. After EDA reduction, the absorption band at 250 nm corresponding to the $\pi \rightarrow \pi^*$ transitions of aromatic [27] redshifts to around 260 nm and the band at ~301 nm corresponding to the $n \rightarrow \pi^*$ transitions of C = O bonds [27] disappears, confirming the restore of sp^2 region upon EDA reduction. Meanwhile, the formation of AgNPs is also confirmed by the UV-vis spectrum of rGO-Ag_H where a maximum adsorbance was observed at ~412 nm [28].

The reduction level of GO investigated by FTIR spectroscopy in detail is shown in Fig. 3. For GO spectrum, the bands at 3410, 1730, 1630, 1280 and 1060 cm^{-1} are assigned to the stretching vibrations of O–H, C = O [29], C = C [30], C–OH [31] and C–O–C [17], respectively. The band at 1400 cm^{-1} emanates from the deformation vibration of C-OH. After reduction, the intensities of these bands decrease evidently, especially the carboxyl and hydroxy groups (1730 and 3447 cm^{-1}). The bands at 3410, 1630, 1400 and 1060 cm^{-1} are up or down shift to 3447, 1657, 1383 and 1114 cm^{-1}, respectively. These changes results from the reduction of GO and the attachment of AgNPs on the surface of rGO sheets. Notably, though their intensities are reduced, a substantial amount of oxygen-containing functional groups are still present on rGO-Ag_H evidently. Two additional bands resulted from the stretching vibration of C-N [32] and N-H arise at 1207 and 1574 cm^{-1}, respectively, due to the substitution reaction between amine groups of EDA and epoxide groups of GO [33]. The oxygen and nitrogen functional groups with lone-pair electrons are generally charged differently. It is reported that the Te(IV) species are highly dependent on pH. The $[Te(OH)_3]^+$, $[TeO(OH)]^+$ and $[TeO_2(OH)_2]^{2-}$ are predominate in water at pH < 2, pH > 4 and pH > 8 [16], respectively. These functional groups might be the potential binding sites of rGO-Ag_H for anchoring the cationic or anionic Te(IV) species in SERS detection experiments.

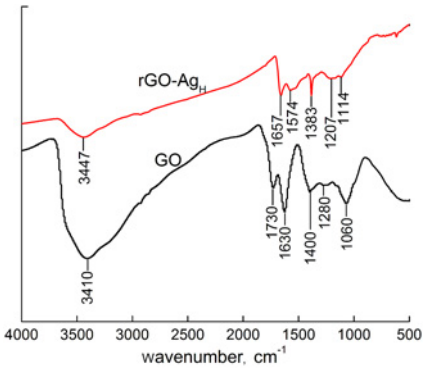

Fig. 3 *FTIR spectroscopy of GO and rGO-Ag_H*

The roles of the functional groups and AgNPs in Te(IV) adsorption investigated by XPS are shown in Fig. 4. After EDA reduction, the relative atomic ratio of O to C, which is determined to be ~0.5 for GO, drops below to 0.2 and the relative atomic ratio of N to C increases to 0.1, which results from the partial reduction of GO and the nitrogen incorporation during EDA reduction (Fig. 4*a*). The O 1s XPS spectrum of GO can be deconvoluted into two peaks, which are associated with C = O (532.4 eV) and C-O (533.2 eV) (Fig. 4*b*). For rGO-Ag_H, they shift to 531.2 and 533.1 eV, respectively. The N 1s spectrum of rGO-Ag_H can also be fitted to two curves with binding energies of 399.1 and 400.0 eV (Fig. 4*c*), which can be ascribed to –CO-NH- and –CH_2-NH_2, respectively [34]. After exposure to Te(IV), the O 1s and N 1s spectra of rGO-Ag_H vary greatly, both in the shapes and positions. The relative intensity between C = O and C-O decreases and their positions further shift

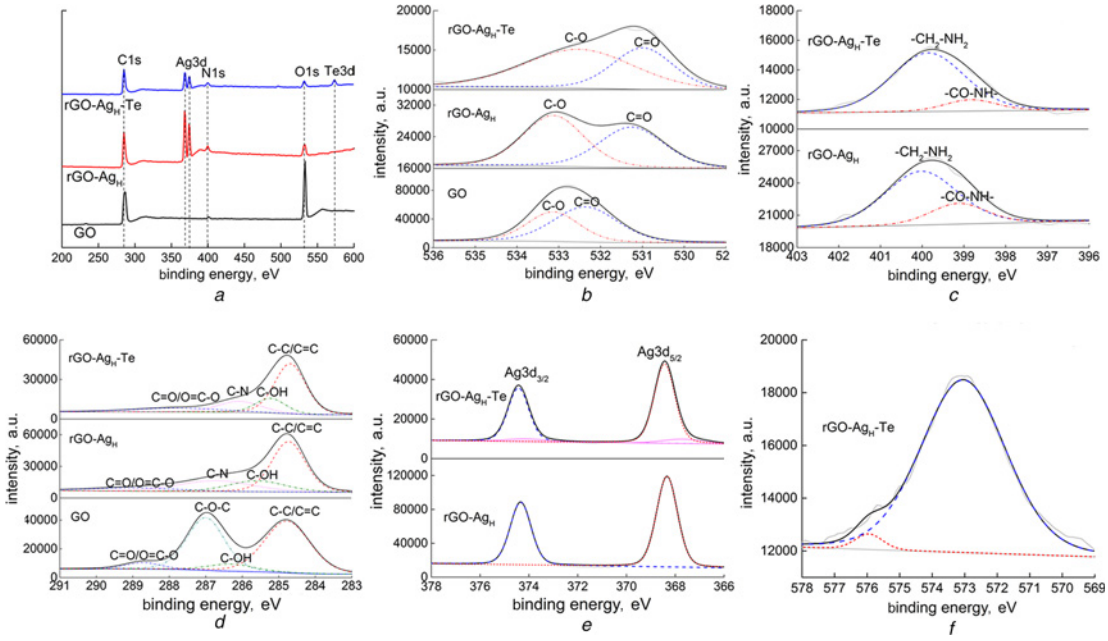

Fig. 4 *Te 3d (f) XPS analysis of GO and rGO-Ag_H obtained before (noted as rGO-Ag_H) and after (noted as rGO-Ag_H-Te) adsorption*
a XPS survey spectra and
b O 1s,
c N 1s,
d C 1s,
e Ag 3d

to 531.0 and 532.5 eV, respectively (the rGO-Ag_H-Te spectrum in Fig. 4*b*). The peak intensity of –CO-NH- increases and the position also varies to 398.8 eV (the rGO-Ag_H-Te spectrum in Fig. 4*c*). The great variations of the O 1s and N 1s spectra provide the evidence that both of the oxygen- and nitrogen-containing functional groups play important roles in Te(IV) adsorption by rGO-Ag_H. The deconvolution of the C 1s peaks of GO and rGO-Ag_H before and after adsorption further confirmed the formation of nitrogen-containing functional groups and the involvement of these functional groups in Te(IV) adsorption (Fig. 4*d*). Figs. 4*e* and *f* shows the fitting of the Ag 3d and Te 3d peaks after Shirley background subtractions, respectively. Two individual peaks occurred at 374.2 ± 0.2 and 368.2 ± 0.2 eV are observed in the Ag 3d XPS spectra obviously. They correspond to the $3d_{3/2}$ and $3d_{5/2}$ binding energies of metallic Ag, respectively[35–37]. After contacting with Te(IV), another two new weak peaks occurred at 374.2 ± 0.2 and 367.8 ± 0.2 eV which result from the Ag(I) 3d binding energies [38] and the strong peak at 573.0 ± 0.2 eV in Te 3d XPS spectrum which corresponds to the Te $3d_{5/2}$ level of Te(II-) suggest the involvement of AgNPs in Te(IV) accumulation through chemical reaction, as reported in previous work [11]. A weak peak at 576.0 ± 0.2 eV is also observed in Te 3d XPS spectrum. It results from the spontaneous deposition of Te(IV) on the surface of AgNPs. The AgNPs on the rGO sheets could serve a dual function, enhancing the Raman spectroscopy as 'hot spots' and accumulating Te(IV) species as 'adsorption sites' through chemical and deposition mechanisms.

The Raman spectrum of Te(IV) stock solution with concentration of 78.4 nM is shown in Fig. 5*a*, where the strong peaks at 517.7 and 940.3 cm^{-1} are attributed to the silicon substrate [39]. At 642.9 and 433.6 cm^{-1}, there are two smeared peaks belonging to Te(IV) oxide [40]. The former of these two peaks was assigned to the totally symmetric combination of the TeO_2 pulsations in Mirgorodsky's research [41]. The latter is ascribed to the symmetric stretching vibrations of Te-O-Te bridges [41]. There are no other peaks in the Raman spectrum of rGO-Ag_H apart from the D and G bands (Fig. 5*b*). Then after exposure to the Te(IV) solution for 5 h, the two bands red shift from 1343.3 and 1587.8 cm^{-1} to 1317.9 and 1584.5 cm^{-1}, respectively (Fig. 5*c*), due to the charge transfer from graphene sheets to the accumulated Te(IV) species. In addition, the band at 433.6 cm^{-1} disappears and a strong band occurs at around 600.0 cm^{-1}, which can be assigned to the vibration of Te-O bond. The stretching Raman band of TeO_2 is enhanced apparently with rGO-Ag_H substrate. The enhancement ratio (ER) can be expressed as follows:

$$ER = I_{\mathrm{rGO-Ag_H-Te(IV)}}/I_{\mathrm{Te(IV)}} \quad (2)$$

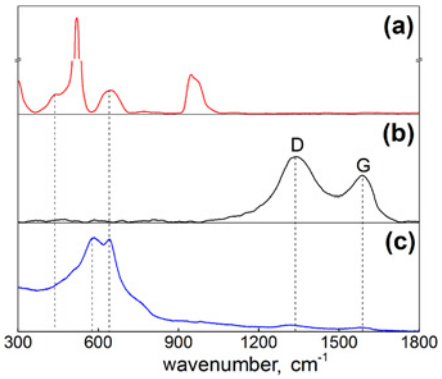

Fig. 5 *Raman spectrum of Te(IV) stock solution with concentration of 78.4 nM*
a Comparative Raman spectra of Te(IV) stock solution
b rGO-Ag_H (b) and
c rGO-Ag_H exposed to Te(IV) solution
(Te(IV) = 78.4 nM, pH = 4.5 ± 0.2)

where *I* represents the peak intensity in the corresponding spectrum. The ER value is calculated to be more than 350, which demonstrates the applicable of the rGO-Ag_H as an effective substrate for SERE detection of trace Te(IV).

The Raman spectra of rGO-Ag_H with Te(IV) accumulation highly depend on the pH of Te(IV) solution (Fig. 6*a*). The D and G bands of rGO-Ag_H occurs at 1332.0 and 1584.7 cm^{-1}, respectively, and the I_D/I_G values continuously increases with decreasing pH (Table 1), which implies that the acidic condition make it easier to form defect on rGO sheets. The symmetric stretching band of O=Te=O only appears in the Raman spectrum of rGO-Ag_H that accumulated Te(IV) at pH 5.5 because of the formation of a large amount of $TeO_2{\cdot}nH_2O$ [42]. The vibration peak of Te-O exhibits in all spectra of rGO-Ag_H that exposed to Te(IV) solution with different pH, even though the Te(IV) species transforms seriously due to the hydrolysis and hydroxyl induced polymerisation [43]. With increasing pH, the peak intensity arise continuously in parallel with the adsorption percentage and reaches the maximum at pH 5.5 (Fig. 6*b*), and then both of them fall simultaneously. The results can be explained by the variation of chemical enhancement

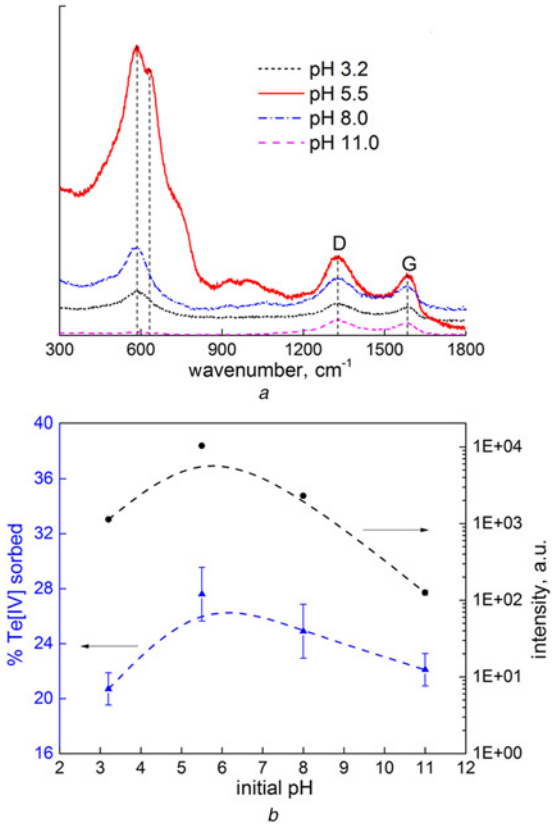

Fig. 6 *Raman spectra of rGO-Ag_H with Te(IV) accumulation highly depend on the pH of Te(IV) solution*
a Raman spectra of rGO-Ag_H exposed to 78.4 nM Te(IV) solution at different pH
b corresponding relationship between the percentage of Te(IV) adsorption and peak intensity of 584.9 cm^{-1}

Table 1 Positions of D and G peaks and their average intensity ratio at different pH calculated on three tested data

Initial pH	3.20	5.50	8.00	11.00
D peak (cm^{-1})	1331.9	1331.9	1332.9	1332.9
G peak (cm^{-1})	1584.7	1584.7	1584.7	1584.7
I_D/I_G	1.37 ± 0.02	1.35 ± 0.01	1.33 ± 0.01	1.16 ± 0.01

doi: 10.1049/mnl.2017.0297

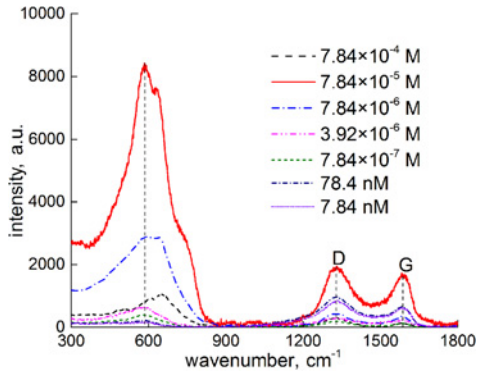

Fig. 7 *Raman spectra of rGO-Ag$_H$ exposed to Te(IV) solution with different concentration*

caused by the change of Te(IV) accumulation, which resulted from the increasing solubility of Te(IV) at both lower and higher pH [40]. Another interesting phenomenon observed in our study is that the position of Te-O stretching vibration peak remains at 584.9 cm^{-1} with varying pH. It is different from uranyl SERS band shifting in Sepaniak's and Dutta's researches [9, 44]. The band hereby is selected as the monitoring signal for trace Te(IV) detection.

The Raman spectra of rGO-Ag$_H$ exposed to Te(IV) with different levels at pH 5.5 are shown in Fig. 7. The stretching band of Te-O occurs at 584.9 cm^{-1}. Its intensity decreases when the concentration of Te(IV) ranges from 7.84×10^{-5} to 7.84×10^{-9} M. This phenomenon can be attributed to the reduction of Te(IV) accumulation on the substrate. At higher concentration, the formation of the monolayer Te(IV) species with dense distribution on the surface of rGO-Ag$_H$ makes the Raman enhancement increases to the maximum. With dilution, the enhanced Raman signal decreases as less charged transfer states of the metal adsorbed molecule complex available on the substrate [9]. It is worth noting that the Raman band of O=Te=O just appears at higher concentration, suggesting the limitation of the band for detection of low-level Te(IV) in aqueous solution. The band intensity achieves a constant at a lower concentration. The detecting limit for Te(IV) is found to be about 100 nM with the use of rGO-Ag$_H$ substrate fabricated by EDA reduction-induced self-assembly.

4. Conclusion: In conclusions, the AgNPs/rGO hydrogel with porous structure, good mechanical and absorbability that are favourable to Te(IV) adsorption and separation is fabricated by a facile one-step reduction-induced self-assembly method. The as prepared rGO-Ag$_H$ is applied as a SERS substrate to monitor trace homologue tellurium of polonium in aqueous solution for the first time. The close packed AgNPs on the surface of rGO offers lots of 'hot spots' for SERS detection and the functionalised rGO-Ag$_H$ serves as an effective adsorbent for tellurium enrichment. The peak of TeO_2 pulsations at 642.9 cm^{-1} is effectively enhanced for more than 350 times, suggesting the validity of rGO-Ag$_H$ as SERS substrate. Distinctly, the characteristic peak of Te-O stretching at 584.9 cm^{-1} keeps constant in rGO-Ag$_H$ spectra with varying pH, which offers a marker for SERS monitoring of trace Te(IV). With the use of rGO-Ag$_H$ designed in a very simple manner, the Raman spectral detection of tellurium(IV) becomes possible despite its complex nature in aqueous solution. A detection limit of about 100 nM is achieved at pH 5.50. According to the similar chemical behaviour of Po(IV) and Te(IV) in aqueous solution, it can be assumed that the rapid detection of trace polonium in radioactive wastewater with high sensitivity using a common instrument becomes possible.

5. Acknowledgments: This work was supported by the National Natural Science Foundation of China (grant no. 21403246) and the Strategic Priority Research Program of Chinese Academy of Science (grant no. XDA03040000).

6 References

[1] Rizzi M., Neuhausen J., Eichler R., *ET AL.*: 'Polonium evaporation from dilute liquid metal solutions', *J. Nucl. Mater.*, 2014, **450**, (1-3), pp. 304–313
[2] Numata Y., Otsuka M., Yamagishi K., *ET AL.*: 'Quantitative determination of glycine, alanine, aspartic acid, glutamic acid, phenylalanine, and tryptophan by Raman spectroscopy', *Anal. Lett.*, 2017, **50**, (4), pp. 651–662
[3] Lee S.Y., Ganbold E.O., Choo J., *ET AL.*: 'Detection of melamine in powdered milk using surface-enhanced Raman scattering with no pretreatment', *Anal. Lett.*, 2009, **43**, (14), pp. 2135–2141
[4] Zhang H., Kang Y., Liu P., *ET AL.*: 'Determination of pesticides by surface-enhanced Raman spectroscopy on gold nanoparticle modified polymethacrylate', *Anal. Lett.*, 2016, **49**, (14), pp. 2268–2278
[5] Lai Y.M., Wang J., He T., *ET AL.*: 'Improved surface enhanced Raman scattering for nanostructured silver on porous silicon for ultrasensitive determination of 2,4,6-trinitrotoluene', *Anal. Lett.*, 2014, **47**, (5), pp. 833–842
[6] Yi Z., Liu M., Luo J.S., *ET AL.*: 'Multiple surface plasmon resonances of square lattice nanohole arrays in Au-SiO_2-Au multilayer films', *Opt. Commun.*, 2017, **390**, pp. 1–6
[7] Liu J.B., Li Y.L., Li Y.M., *ET AL.*: 'Noncovalent DNA decorations of graphene oxide and reduced graphene oxide toward water-soluble metal–carbon hybrid nanostructures via self-assembly', *J. Mater. Chem.*, 2010, **20**, (5), pp. 900–906
[8] Wang G.Q., Chen L.X.: 'Aptameric SERS sensor for Hg^{2+} analysis using silver nanoparticles', *Chinese Chem. Lett.*, 2009, **20**, (12), pp. 1475–1477
[9] Dutta S., Ray C., Sarkar S., *ET AL.*: 'Silver nanoparticle decorated reduced graphene oxide (rGO) nanosheet: a platform for SERS based low-level detection of uranyl Ion', *ACS Appl. Mater. Inter.*, 2013, **5**, (17), pp. 8724–8732
[10] Ruan C.M., Luo W.S., Wang W., *ET AL.*: 'Surface-enhanced Raman spectroscopy for uranium detection and analysis in environmental samples', *Anal. Chim. Acta*, 2007, **605**, (1), pp. 80–86
[11] Zhou X.J., Wang C., Huang H., *ET AL.*: 'Extensive adsorption of the lighter homologue tellurium of polonium from wastewater using porous silver layer deposited stainless steel mesh', *Prog. Nucl. Energ.*, 2017, **98**, pp. 285–292
[12] Jiao T.F., Guo H.Y., Zhang Q.R., *ET AL.*: 'Reduced graphene oxide-based silver nanoparticle-containing composite hydrogel as highly efficient dye catalysts for wastewater treatment', *Sci. Rep.*, 2015, **5**, (11873), pp. 1–12
[13] Buongiorno J., Loewen E.P., Czerwinski K., *ET AL.*: 'Studies of polonium removal from molten lead-bismuth for lead-alloy-cooled reactor applications', *Nucl. Technol.*, 2004, **147**, (3), pp. 406–417
[14] Ermolaev N., Bugreev M., Yefimov E.: 'Methods of removal and containment of radioactive polonium from lead-bismuth coolant'. Proc. Heavy Liquid Metal Coolants in Nuclear Technology (HLMC-98), Obninsk, Russia, 1998, pp. 194–200
[15] Starik I.E., Ampelogova N.I., Kuznetsov B.S.: 'Hydrolysis of polonium in perchloric acid', *Radiokhimiya*, 1964, **6**, (1), pp. 519–524
[16] Ayala R., Martínez J.M., Pappalardo R.R., *ET AL.*: 'Quantum-mechanical study on the aquaions and hydrolyzed species of Po(IV), Te(IV), and Bi(III) in water', *J. Phys. Chem. B*, 2012, **116**, (51), pp. 14903–14914
[17] Han Z., Tang Z.H., Li P., *ET AL.*: 'Ammonia solution strengthened three-dimensional macro-porous graphene aerogel', *Nanoscale*, 2013, **5**, (12), pp. 5462–5467
[18] Qiu L., Liu J.Z., Chang S.L.Y., *ET AL.*: 'Biomimetic superelastic graphene-based cellular monoliths', *Nat. Commun.*, 2012, **3**, (1241), pp. 1–7
[19] Li J.H., Li J.Y., Meng H., *ET AL.*: 'Ultra-light, compressible and fire-resistant graphene aerogel as a highly efficient and recyclable absorbent for organic liquids', *J. Mater. Chem. A*, 2014, **2**, (9), pp. 2934–2941
[20] Kennedy B.J., Spaeth S., Dickey M., *ET AL.*: 'Determination of the distance dependence and experimental effects for modified SERS substrates based on self-assembled monolayers formed using alkanethiols', *J. Phys. Chem. B*, 1999, **103**, (18), pp. 3640–3646
[21] Xu H., Aizpurua J., Kall M., *ET AL.*: 'Electromagnetic contributions to single-molecule sensitivity in surface-enhanced Raman scattering', *Phys. Rev. E*, 2000, **62**, (3), pp. 4318–4324

[22] Das M.R., Sarma R.K., Saikia R., *ET AL.*: 'Synthesis of silver nanoparticles in an aqueous suspension of graphene oxide sheets and its antimicrobial activity', *Colloid Surface B*, 2011, **83**, (1), pp. 16–22
[23] Yi Z., Xu X.B., Fang Q., *ET AL.*: 'Fabrication of silver nanosheets on quartz glass substrates through electroless plating approach', *Appl. Phys. A*, 2014, **114**, (2), pp. 485–493
[24] Li Y.J., Gao W., Ci L.J., *ET AL.*: 'Catalytic performance of Pt nanoparticles on reduced graphene oxide for methanol electro-oxidation', *Carbon*, 2010, **48**, (4), pp. 1124–1130
[25] Saito Y., Yoshikawa T.: 'Interlayer spacings in carbon nanotubes', *Phys. Rev.*, 1993, **48**, (3), pp. 1907–1909
[26] Fan Z.J., Wang K., Wei T., *ET AL.*: 'An environmentally friendly and efficient route for the reduction of graphene oxide by aluminum powder', *Carbon*, 2010, **48**, (5), pp. 1686–1689
[27] Pham V.H., Cuong T.V., Hur S.H., *ET AL.*: 'Chemical functionalization of graphene sheets by solvothermal reduction of a graphene oxide suspension in N-methyl-2-pyrrolidone', *J. Mater. Chem.*, 2011, **21**, (10), pp. 3371–3377
[28] Justin Packia Jacob S., Finub J.S., Narayanan A.: 'Synthesis of silver nanoparticles using Piper longum leaf extracts and its cytotoxic activity against Hep-2 cell line', *Colloid Surface B*, 2012, **91**, (2), pp. 212–214
[29] Wang R.H., Wang Y., Xu C.H., *ET AL.*: 'Facile one-step hydrazine-assisted solvothermal synthesis of nitrogen-doped reduced graphene oxide: Reduction effect and mechanisms', *RSC Adv.*, 2013, **3**, (4), pp. 1194–1200
[30] Duan F.F., Chen C.Q., Wang G.Z., *ET AL.*: 'Efficient adsorptive removal of dibenzothiophene by graphene oxide-based surface molecularly imprinted polymer', *RSC Adv.*, 2014, **4**, (3), pp. 1469–1475
[31] Paredes J.I., Villar-Rodil S., Martinez-Alonso A., *ET AL.*: 'Graphene oxide dispersions in organic solvents', *Langmuir*, 2008, **24**, (19), pp. 10560–10564
[32] Ma H.L., Zhang Y.W., Hu Q.H., *ET AL.*: 'Chemical reduction and removal of Cr(VI) from acidic aqueous solution by ethylenediamine-reduced graphene oxide', *J. Mater. Chem.*, 2012, **22**, (13), pp. 5914–5916
[33] Bourlinos A.B., Gournis D., Petridis D., *ET AL.*: 'Graphite oxide: chemical reduction to graphite and surface modification with primary aliphatic amines and amino acids', *Langmuir*, 2003, **19**, (15), pp. 6050–6055
[34] Yan J.L., Chen G.J., Cao J., *ET AL.*: 'Functionalized graphene oxide with ethylenediamine and 1,6-hexanediamine', *New Carbon Mater.*., 2012, **27**, (5), pp. 370–376
[35] Zhan B.B., Liu C.B., Shi H.X., *ET AL.*: 'A hydrogen peroxide electrochemical sensor based on silver nanoparticles decorated three-dimensional graphene', *Appl. Phys. Lett.*, 2014, **104**, (24), pp. 243704
[36] Zhang D.H., Liu X.H., Wang X.: 'Green synthesis of graphene oxide sheets decorated by silver nanoprisms and their anti-bacterial properties', *J. Inorg. Biochem.*, 2011, **105**, (9), pp. 1181–1186
[37] Yi Z., Xu X.B., Kang X.L., *ET AL.*: 'Fabrication of well-aligned ZnO@Ag nanorod arrays with effective charge transfer for surface-enhanced Raman scattering', *Surf. Coat. Tech.*, 2017, **324**, pp. 257–263
[38] Zuo P.F., Zhang S.G., Jin B.K., *ET AL.*: 'Rapid synthesis and electrochemical property of Ag_2Te nanorods', *J. Phys. Chem. C*, 2008, **112**, (38), pp. 14825–14829
[39] Condrate R.A.Sr.: 'Infrared and Raman spectra of glasses containing rare earth ions', *Key Eng. Mater.*, 1994, **94–95**, (5), pp. 209–232
[40] Maskaeva L.N., Zarubina I.V., Vovkotrubb E.G., *ET AL.*: 'Conditions of hydrochemical synthesis, composition, and structure of tellurium films', *Russ. J. Appl. Chem.*, 2012, **85**, (5), pp. 731–735
[41] Mirgorodsky A.P., Merle-Mejean T., Champarnaud J.C., *ET AL.*: 'Dynamics and structure of TeO_2 polymorphs: model treatment of paratellurite and tellurite; Raman scattering evidence for new γ- and δ-phases', *J. Phys. Chem. Solids*, 2000, **61**, (4), pp. 501–509
[42] Cheng K.L.: 'Analysis of lead telluride with an accuracy to better than 0.1%', *Anal. Chem.*, 1995, **33**, (6), pp. 761–764
[43] McPhail D.C.: 'Thermodynamic properties of aqueous tellurium species between 25 and 350°C', *Geochim. Cosmochim. Ac.*, 1995, **59**, (5), pp. 851–866
[44] Bhandari D., Wells S.M., Retterer S.T., *ET AL.*: 'Characterization and detection of uranyl ion sorption on silver surfaces using surface enhanced Raman spectroscopy', *Anal. Chem.*, 2009, **81**, (19), pp. 8061–8067

doi: 10.1049/mnl.2017.0297